Energetics of pilot-wave hydrodynamics: Nonresonant effects

Tino Damiani [1], Matthew Durey [2], Bauyrzhan K. Primkulov [3] and John W. M. Bush [1,*]

[1] *Department of Mathematics, Massachusetts Institute of Technology, Cambridge, Massachusetts 02139, USA*

[2] *School of Mathematics and Statistics, University of Glasgow, University Place, Glasgow G12 8QQ, United Kingdom*

[3] *Department of Mechanical Engineering, Yale University, New Haven, Connecticut 06511, USA*

(Received 16 December 2025; accepted 20 July 2026; published 12 August 2026)

A millimetric droplet can bounce indefinitely on a vertically vibrating bath and generate a Faraday pilot-wave field that propels it forward. This hydrodynamic pilot-wave system, in which a walking droplet is accompanied by its quasi-monochromatic wave field, exhibits several features previously thought to be exclusive to the quantum realm. For steady dynamical states, the energy input from the vibrational forcing and output from viscous dissipation must balance, so one can consider the partitioning between the droplet and wave energy. The energetics of the hydrodynamic pilot-wave system have been considered only in the special case where there is resonance between the bouncing drop and its pilot wave, so one may neglect the drop's vertical dynamics. We here deepen our understanding of pilot-wave energetics by simulating these vertical dynamics, allowing us to assess the energetics of both resonant and nonresonant walking states. Specifically, we characterize the dependence of the system energetics on the droplet's bouncing or walking mode, and assess whether resonance has a significant influence on the partitioning between drop and wave energy. In all instances, the horizontal kinetic energy of the drop is negligible relative to its gravitational potential energy. At high memory, where the pilot waves are most persistent, the pilot-wave energy dominates the total system energy, exceeding the droplet energy by an order of magnitude. When the resonance between drop and wave is broken, the wave energy is slightly diminished due to wave interference, but remains dominant.

DOI: 10.1103/fpg5-myb3

I. INTRODUCTION

The hydrodynamic pilot-wave system [1] was discovered in 2005 by Yves Couder and Emmanuel Fort [2,3]. It consists of a millimetric droplet self-propelling on the surface of a vibrating bath, driven forward through an interaction with its own wave field. This system reproduces many phenomena previously thought to be exclusive to the microscopic quantum domain, and represents a macroscopic realization of wave-particle duality of the form envisaged by de Broglie in his double-solution pilot-wave theory [4,5]. It forms the basis of the field of hydrodynamic quantum analogs, the goal of which is to redefine the boundary between classical and quantum systems [6,7].

When a liquid bath is vibrated vertically at angular frequency $\omega = 2\pi f$ with a vibrational acceleration, γ, that exceeds the Faraday threshold, γ_F, its surface becomes unstable to a standing field of Faraday waves with frequency $\omega_F = \omega/2$ and wavelength λ_F prescribed by the water wave dispersion relation [8,9]. The hydrodynamic pilot-wave system is achieved by placing a millimetric drop on the surface of a vertically vibrated bath for which $\gamma_B < \gamma < \gamma_F$, where γ_B denotes the bouncing threshold, the minimum bath acceleration required to preclude the drop's

*Contact author: bush@math.mit.edu

TABLE I. Relevant parameters and variables of the pilot-wave model and its energetics [13,15,16,33].

Parameter	Definition
R, $m = \frac{4}{3}\pi\rho R^3$, ρ, σ	Drop radius, mass, oil density, and surface tension
μ_a, μ_e	Air and effective oil dynamic viscosity [13]
$\omega = 2\pi f$, $\omega_F = \frac{1}{2}\omega$	Angular driving frequency, Faraday angular frequency
γ, γ_F	Vibrational acceleration and Faraday threshold
$\omega_D = \sqrt{\sigma/\rho R^3}$, $\Omega = \omega/\omega_D$	Drop natural frequency and vibration number
λ_F, k_F, T_F	Faraday wavelength, wave number, and period
z_p, $\boldsymbol{x}_p$	Droplet height and horizontal position
$h(\boldsymbol{x},t)$, $\mathscr{H}(\lvert\boldsymbol{x}\rvert)$	Wave field and wave kernel
T_c	Droplet contact time interval with the bath
$T_D = \rho/(\mu_e k_F^2)$	Wave decay time [13]
$\mathrm{Me} = \frac{T_D}{T_F(1-\gamma/\gamma_F)}$	Memory parameter
$F_N(t)$	Normal force during impact
$\mathcal{D}_h = 0.17$, $\mathcal{D}_v = 0.48$	Horizontal and vertical drag coefficients
$\mathcal{C}_v = 0.59$	Vertical dynamics' spring constant
$\Phi_F = \frac{\int_{T_c} F_N(s)\omega_F s\ \mathrm{d}s}{\int_{T_c} F_N(s)\ \mathrm{d}s} \bmod(2\pi)$	Phase parameter
$\alpha = \frac{\rho\epsilon^2}{2\mu_e(1+2\epsilon^2)}$, $\epsilon = \frac{\omega\mu_e k_F}{3k_F^2\sigma+\rho g}$	Spatial damping factor and wave number correction
$l_d = \frac{1}{2}\sqrt{T_F \mathrm{Me}/\alpha}$	Spatial decay length
$\overline{E}_p$, $\overline{E}$	Droplet energy and pilot-wave energy
H	Stroboscopic wave amplitude at impact

coalescing with the bath. In this regime, the droplet bounces indefinitely while the surface waves are generated entirely by the droplet [10,11]. The vibrational acceleration prescribes the decay time of the waves on the surface, and thus the "memory" of the system. The memory parameter, Me (see Table I), determines the number of previous bounces that will influence the droplet [12]. As the vibrational acceleration increases towards γ_F, the droplet destabilizes into a dynamic walking state, propelled forward by its wave field at mean horizontal speed v. The behavior of the droplets has been characterized in terms of its dependence on two nondimensional parameters [13,14]. The first is the drop's vibration number, $\Omega = \omega/\omega_D$, a proxy for drop size, where $\omega_D = \sqrt{\sigma/\rho R^3}$ is proportional to the drop's natural frequency [15]. The second is the nondimensional vibrational acceleration, $\Gamma = \gamma/g$, of the bath, which prescribes the longevity of the wave field and so the system memory, Me.

For much of the Ω-Γ parameter space considered, the drop executes periodic bouncing or walking states, and so is locked in resonance with the Faraday frequency, ω_F. However, at high memory and for certain drop sizes the resonance between drop and pilot wave is lost: the droplet's bouncing becomes aperiodic, and "nonresonant" bouncing or walking states emerge [14]. For example, chaotic bouncing and walking regimes arise in which the vertical drop dynamics are unpredictable. Intermittent walking regimes arise in which the drop never reaches a steady walking speed, but instead moves intermittently along a straight line, with sporadic reversals in direction [3,13,14,16]. Perrard *et al.* [17] demonstrated that the walker system is reversible: specifically, "time reversal" occurs when the droplet undergoes a phase flip of π, thereby changing directions. In backtracking along its original trajectory, it erases its wave field through destructive interference, thus largely nullifying its wave energy. The question naturally arises as to how the wave energy changes when resonance is lost: does the impact phase variability substantially decrease the wave energy via interference?

The hydrodynamic pilot-wave system is driven and dissipative, with injection of energy by the bath vibration, and loss of energy through viscous dissipation. Nevertheless, steady states arise in the hydrodynamic pilot-wave system, including steady bouncing and walking states [2,13,15], as

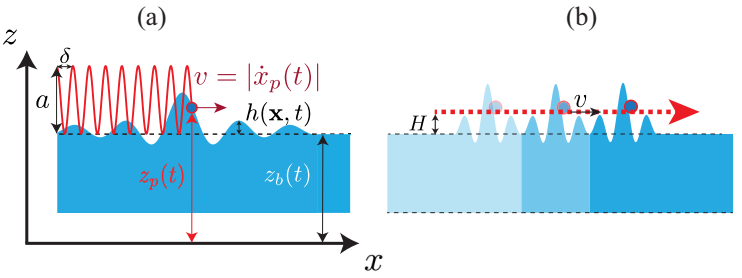

FIG. 1. Physical picture of the hydrodynamic pilot-wave system in the case of a resonant (2,1) walker, which bounces once per Faraday period. (a) Schematic of the full dynamics of the droplet, including its fast-time-scale bouncing. (b) Schematic illustrating the stroboscopic approximation. H is the local height of the wave field time-averaged over impact, and mgH thus represents a stroboscopic proxy for the drop's gravitational potential energy.

well as periodic orbital states [3,18–22]. In such states, there is a balance between the energy input via bath vibration and energy loss through viscous dissipation. For these, we can neglect the global energetics of the system and focus on the energy partitioning between the droplet and wave field.

If one considers a resonant steady walker and strobes the system once per bounce cycle at ω_F, the droplet appears to glide along the bath surface, dressed in a quasi-monochromatic pilot wave that is stationary in the droplet's frame of reference [23,24]. The drop dynamics in this strobed frame are well described by the stroboscopic model [23,25], in which the vertical drop dynamics are averaged, and so eliminated from consideration. This averaging allows for a simplified treatment of the system, and the stroboscopic model has been successful in describing many of the features of the pilot-wave system, including the stability of walking and orbiting states [22,23,26–28].

To date, the energetics of the hydrodynamic pilot-wave system have been studied only in the context of resonant walkers [26,29–31]. The wave energy associated with droplets walking in a central force has been well characterized [18,22], and Hubert *et al.* [32] highlighted the role of wave interference arising at high memory. In their analysis of the stroboscopic model [23], Durey and Bush [33] derived simple relationships between the droplet's horizontal kinetic energy, its gravitational potential energy and the wave energy. However, the stroboscopic model does not treat the droplet's vertical dynamics; consequently the drop's gravitational potential energy can be only assessed at the time of impact (Fig. 1). Moreover, nonresonant effects and their impact on the energy partitioning cannot be analyzed. The stroboscopic approximation thus precludes a full characterization of the droplet energy, and motivates the use of a model that explicitly treats the vertical dynamics.

A complete description of the system energetics requires consideration of the fully three-dimensional droplet dynamics. By adapting the models developed by Moláček and Bush [13] and Primkulov *et al.* [16], we here characterize all of the relevant system energies: the gravitational potential energy and vertical kinetic energy of the droplet, its horizontal kinetic energy as prescribed by its walking speed, and the energy associated with its pilot wave. We thus quantify the partitioning between wave and droplet energy for both resonant and nonresonant states, allowing for an assessment of the effect of resonance on this partitioning.

In Sec. II we detail the theoretical model that we use to investigate the system energetics. In Sec. III we characterize the energetic partitioning of the system in various bouncing and walking regimes. We examine how this partitioning changes with vibrational acceleration of the bath and drop size, and how it depends on wave-droplet resonance. In Sec. IV we compare our results with those obtained from the stroboscopic model in order to better understand the role of the vertical dynamics on the system energetics. Finally, in Sec. V we compare the energetics of our system to those proposed in de Broglie's double-solution pilot-wave theory of quantum dynamics.

II. COUPLED WALKER MODEL

A. Physical picture

Figure 1 illustrates the hydrodynamic pilot-wave system. The bath is driven at frequency $f = \omega/2\pi$ and acceleration γ, corresponding to a vibration amplitude of γ/ω^2. Figure 1(a) illustrates the full dynamics of a resonant walker, which bounces with the frequency $\omega_F = \omega/2$ of the most unstable Faraday waves. We describe the dynamics in the laboratory frame of reference; thus, the unperturbed bath surface moves according to $z_b(t) = -(\gamma/\omega^2)\sin(\omega t)$. The height of the walker's base is denoted $z_p(t)$, so that $z_p(t) - z_b(t)$ represents its height above the unperturbed bath surface. The walker bounces with characteristic vertical amplitude a. Each impact of the droplet on the bath generates surface standing waves, and $h(\boldsymbol{x}, t)$ denotes the surface perturbation from $z_b(t)$. Consideration of the vertical dynamics of the droplet allows one to characterize the phase of impact, Φ_F, of the drop relative to the bath oscillation (as defined in Table I), and this phase becomes variable in the presence of nonresonant effects. It has previously been shown that the inclusion of a variable impact phase provides a better understanding of a number of phenomena such as collinear swaying at the onset of motion, intermittent walking, and chaotic speed oscillations [13,14,16], in addition to the subtle interactions of droplet pairs [34–38].

At each impact with the bath, the droplet receives a small horizontal impulse from its pilot wave and is propelled forward by a horizontal step of characteristic amplitude $\delta \ll a$ at the walking speed $v = |\dot{\boldsymbol{x}}_p|$. Note that during a period of the droplet's vertical dynamics (which for steady resonant walkers is the Faraday period $T_F = 2/f$), one expects the dominant energy exchange to be between the drop's gravitational potential energy and vertical kinetic energy. The horizontal kinetic energy scales as $\sim\frac{1}{2}m(\delta/T_F)^2$ and the vertical kinetic energy as $\sim\frac{1}{2}m(2a/T_F)^2$, so their ratio scales as $\sim(\delta/2a)^2 \ll 1$. One thus expects the horizontal kinetic energy of the drop to be small relative to both its vertical kinetic energy and gravitational potential energy. The partitioning between the drop energy and wave energy is less obvious, but will be elucidated in Sec. III.

Figure 1(b) illustrates the idealized stroboscopic pilot-wave dynamics, in which the system is strobed at the Faraday frequency, revealing a droplet surfing its pilot wave. Perfect resonance between drop and pilot wave is thus assumed, as is a constant impact phase, Φ_F. The vertical dynamics of the droplet are averaged and all information concerning the height and velocity of the drop during flight is lost, thereby prohibiting the characterization of the droplet's vertical kinetic energy and gravitational potential energy. For this stroboscopic formulation, Durey and Bush [33] defined a proxy for gravitational potential energy, mgH, in terms of the height, H, of the pilot wave time-averaged over the drop impact. The kinetic energy of the drop was described entirely in terms of its horizontal kinetic energy. The dominant droplet energetic balance associated with the vertical dynamics was thus necessarily absent in the stroboscopic model, but will be considered here.

B. Governing equations

We adopt the theoretical model of Primkulov *et al.* [16] as is based on that of Moláček and Bush [13]. The vertical dynamics of the drop are described by

$$m\ddot{z}_p(t) = F_N(t) - mg, \tag{1}$$

where z_p denotes the height of the base of the droplet, m the mass of the droplet, and g the gravitational acceleration. The impact force acting on the drop is given by

$$F_N(t) = \frac{4}{3}\pi\sigma\mathcal{H}(-z_p + z_b + h)\left[\mathcal{D}_v\sqrt{\frac{\rho R^3}{\sigma}}(\dot{z}_p - \dot{z}_b - \dot{h}) + \mathcal{C}_v(z_p - z_b - h)\right]. \tag{2}$$

The Heaviside function $\mathcal{H}(-z_p + z_b + h)$ ensures that the interfacial force acts only when the droplet is in contact with the bath. This force consists of a damping and a spring component, with $\mathcal{C}_v$ and $\mathcal{D}_v$ the spring and damping constants. The vertical dynamics of the drop thus follow the linear spring model developed by Moláček and Bush [15].

We note that Moláček and Bush [13] and Wind-Willassen *et al.* [14] adopted a logarithmic spring model to explain discrepancies between their linear spring model and the observed mode transitions in experiments. However, Couchman *et al.* [35] pointed out that these discrepancies can more readily be explained by the omission of the influence of surface waves on the drop's vertical dynamics, which becomes significant at high memory, Me. The linear spring model was then adopted by Primkulov *et al.* [16] in conjunction with a two-way droplet-wave coupling, which successfully rationalized many complexities of the system's dynamics, including nonresonant effects [16]. We thus adopt the linear spring model and also consider the time-dependent wave height, $h(\boldsymbol{x}_p, t)$, in the characterization of the normal force.

The horizontal dynamics are described by

$$m\ddot{\boldsymbol{x}}_p(t) + \left(\mathcal{D}_h\sqrt{\frac{\rho R}{\sigma}}F_N(t) + 6\pi R\mu_a\right)\dot{\boldsymbol{x}}_p(t) = -F_N(t)\nabla h(\boldsymbol{x}_p, t), \tag{3}$$

where $\boldsymbol{x}_p(t)$ is the drop's horizontal position. The droplet motion is driven by horizontal impulses proportional to the local gradient of the wave field, and resisted by drag incurred at impact and during flight. Finally, the time-dependent wave field generated by the last n impacts is described (for $t > t_n$) by

$$h(\boldsymbol{x}, t) = \cos(\omega_F t)\sum_{i=1}^{n} A_i \frac{\mathrm{e}^{-(t-t_i)/(T_F\,\mathrm{Me})}}{\sqrt{t-t_i}}\mathscr{H}(|\boldsymbol{x}-\boldsymbol{x}_i|), \tag{4}$$

where $\boldsymbol{x}_i$ is the droplet position at each impact time, t_i. The memory parameter $\mathrm{Me} = \frac{T_D}{T_F}(1-\frac{\gamma}{\gamma_F})^{-1}$ is prescribed by the proximity of γ to the Faraday threshold, γ_F, and determines the decay rate of the pilot wave. Here T_D denotes the decay time of the waves with Faraday wavelength λ_F in the absence of vibrational forcing (see Table I). We use the axisymmetric wave kernel

$$\mathscr{H}(r) = \mathrm{J}_0(k_F r)\left[1 + \left(\frac{r}{l_d}\mathrm{K}_1(r/l_d) - 1\right)\mathrm{e}^{-1/(k_F r)^2}\right]$$

developed by Couchman *et al.* [35]. The Bessel function J_0 of the first kind of order zero encodes the radial oscillation in $r = |\boldsymbol{x}|$ over the Faraday wavelength, $\lambda_F = 2\pi/k_F$, while the modified Bessel function K_1 of the second kind of order one encodes the far-field exponential decay over the length scale $l_d = \frac{1}{2}\sqrt{T_F\mathrm{Me}/\alpha}$ (with α defined in Table I). Notably, the spatial decay length increases with the system memory. The wave field oscillates at the angular frequency $\omega_F = \frac{1}{2}\omega$, and we sum over the n previous impacts of the droplet with impact times t_i. Each single standing wave has amplitude [16]

$$A_i = \frac{k_F^3\sqrt{2\mu_e/\pi\rho}}{3k_F^2\sigma + \rho g}\int_{T_c} F_N(s)\sin(\omega_F s)\,\mathrm{d}s, \tag{5}$$

with T_c being the duration of the droplet's ith contact with the bath.

C. Benchmarking model dynamics against existing regime diagrams

By considering both the vertical and horizontal drop dynamics, we can characterize the energetics of different bouncing modes of the droplet. Both bath and droplet consist of silicone oil with kinematic viscosity $\nu = 20$ cSt, density $\rho = 949$ kg/m^3, and surface tension $\sigma = 20.6$ mN/m. We begin by benchmarking our model against prior experimental studies characterizing the bouncing and walking states of the drop. We denote a bouncing mode as $(n_p, n_b)^k$ when the droplet bounces n_b distinct times over the course of n_p vibrational periods of the bath [15,39]. Resonant walkers, such as those illustrated schematically in Fig. 1, are thus denoted as (2,1) walkers. Superscripts k are used to distinguish different states with the same periodicity, with larger k denoting a higher

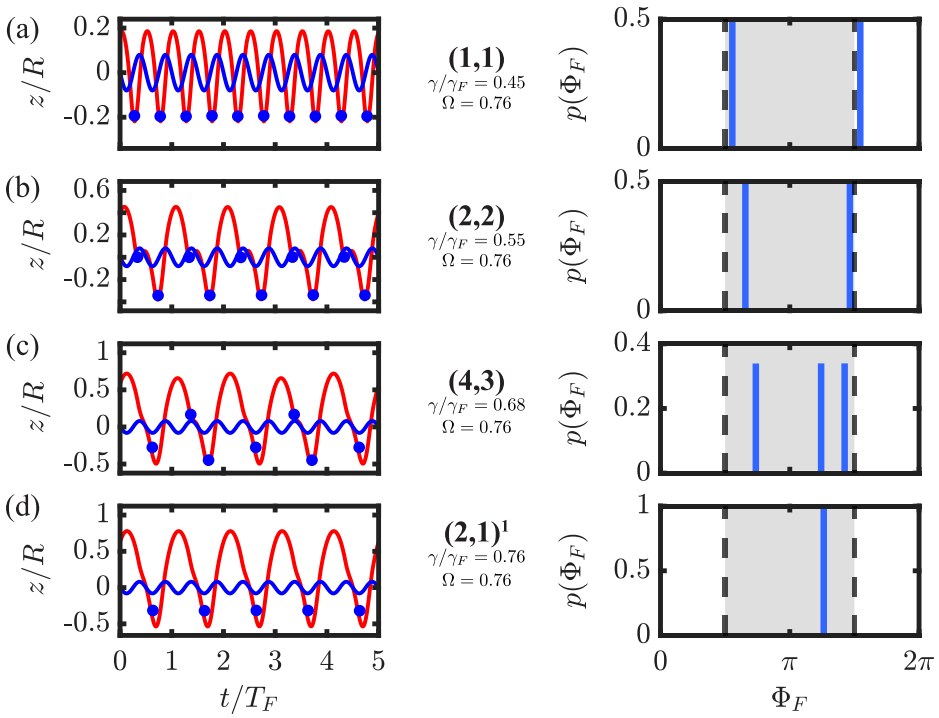

FIG. 2. Depiction of the drop's vertical dynamics (left column) and probability distribution of the impact phase (right column) for different periodic bouncing modes: (a) (1,1) mode, (b) (2,2) mode, (c) (4,3) mode, and (d) a resonant $(2, 1)^1$ mode. In the left column, the height z is scaled by the droplet radius, R. The vertical trajectory of the droplet is depicted in red, the position of the unperturbed bath in blue, and impact times, t_i, are denoted by blue dots. Each mode has a number of distinct impact phases. In (d) we observe the particularity of a resonant mode, where impacts now occur with subharmonic frequency $\omega/2$, and two possible states are accessible that differ only by a phase shift of π. The black dashed lines in the right column correspond to $\Phi_F = \pi/2$ and $\Phi_F = 3\pi/2$, delimitating the regions of the (2,1) droplet's two possible states. At these impact phases, the pilot wave is flat.

energy state. Following Primkulov *et al.* [16], we define a phase parameter

$$\Phi_F = \frac{\int_{T_c} F_N(s)\omega_F s \, \mathrm{d}s}{\int_{T_c} F_N(s) \, \mathrm{d}s} \bmod(2\pi)$$

that characterizes the impact phase of the droplet relative to the bath vibration.

In Fig. 2 we depict (1,1), (2,2), (4,3), and $(2, 1)^1$ bouncing modes. Note that a resonant walker bounces subharmonically (at angular frequency $\omega/2$) with respect to the driving angular frequency ω; consequently, there are two distinct bouncing states that have opposite phase with respect to the bath driving. Adopting the conventions of Primkulov *et al.* [16], the regions $\Phi_F \in [\pi/2, 3\pi/2]$ and $\Phi_F \in [0, \pi/2) \cup (3\pi/2, 2\pi)$ delimit the two possible bouncing states, where phases $\pi/2$ and $3\pi/2$ correspond to a flat interface at impact, and so no horizontal impulse applied to the drop. A lone steady (2,1) walker exhibits the same behavior if its phase relative to the driving is shifted by π, however interaction between several such droplets is highly dependent on their relative phases [34,36,40,41], as is the interaction between a droplet and a standing wave field [42].

It is evident in Fig. 2 that the (1,1) mode bounces twice during a Faraday period, at phases that differ by π. Conversely the (2,2) mode has two distinct impact phases, and the (4,3) mode has three. We observe that as the droplet transitions to a (2,1) mode, subharmonic resonance is achieved

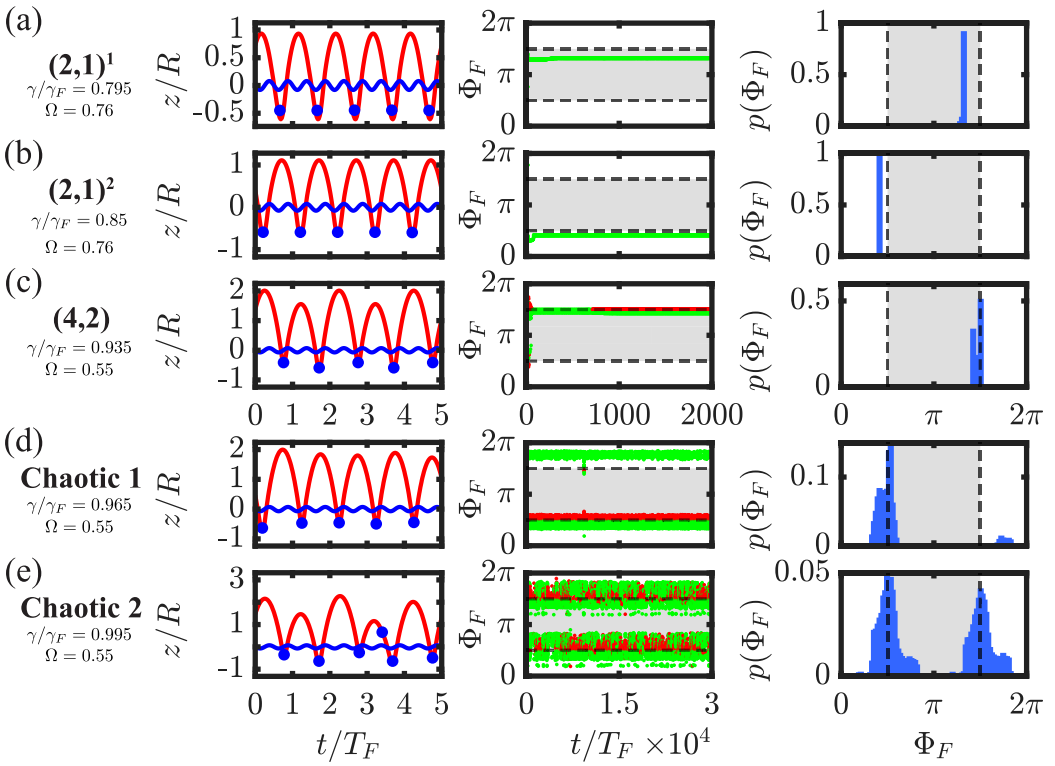

FIG. 3. The drop's vertical dynamics (left column), bouncing phase evolution (middle column), and phase probability distribution (right column) for different walking states: (a) resonant $(2,1)^1$ mode, (b) resonant $(2,1)^2$ mode, (c) resonant (4,2) mode, (d) chaotic 1 mode, and (e) chaotic 2 mode. As the vibrational forcing increases progressively, the $(2,1)^1$ mode (a) transitions into a $(2,1)^2$ mode (b), then a (4,2) mode (c), then chaotic modes (d) and (e). Following the period doubling from mode $(2,1)^2$ to (4,2), two phases emerge near the value of the $(2,1)^2$ phase. Note that the transients in the periodic modes are retained in the central column but not in the rightmost column. In the chaotic modes (d) and (e) the impact phase becomes more widely distributed. The phases in chaotic mode 1 (d) are still concentrated around the $(2,1)^2$ impact phase, and no phase flips are observed. The phases in chaotic mode 2 (e) are more widely distributed, and phase flips (phase shifts of π) arise that are associated with a reversal in walking direction. The left and right columns follow the same nomenclature as in Fig. 2.

between the droplet and wave and the droplet now bounces only once per Faraday period, with a single impact phase. The (2,1) walker observed in Fig. 2(d) is in one of its two possible states ($\pi/2 < \Phi_F < 3\pi/2$), but it could equivalently have locked into the other, with its phase shifted by π.

Figure 3 depicts various walking modes, specifically (2,1) and (4,2) walkers, and two different chaotic walking states denoted by "chaotic 1" and "chaotic 2." In the time series plots, green markers denote impacts that prompt droplet acceleration, while red markers denote impacts that prompt deceleration. We note that the (2,1) walker has the peculiarity of two distinct modes, $(2,1)^1$ and $(2,1)^2$, which have different impact phases and mechanical energies [13,15]. The $(2,1)^2$ walker begins as a $(2,1)^1$ walker before transitioning into a stable $(2,1)^2$ walker, at the point marked by the discontinuity in the impact phase. Each impact of the $(2,1)^1$ and $(2,1)^2$ walkers is marked in green and so propels the droplet forward. The (4,2) walker starts as a $(2,1)^2$ walker before period doubling into a (4,2) mode, in which one of the impacts propels it forward while the other slows it down. Finally, we examine two chaotic modes in Figs. 3(d) and 3(e). In the first, the impact phases are no longer discrete but are concentrated around the initial $(2,1)^2$ impact phase. No π-phase

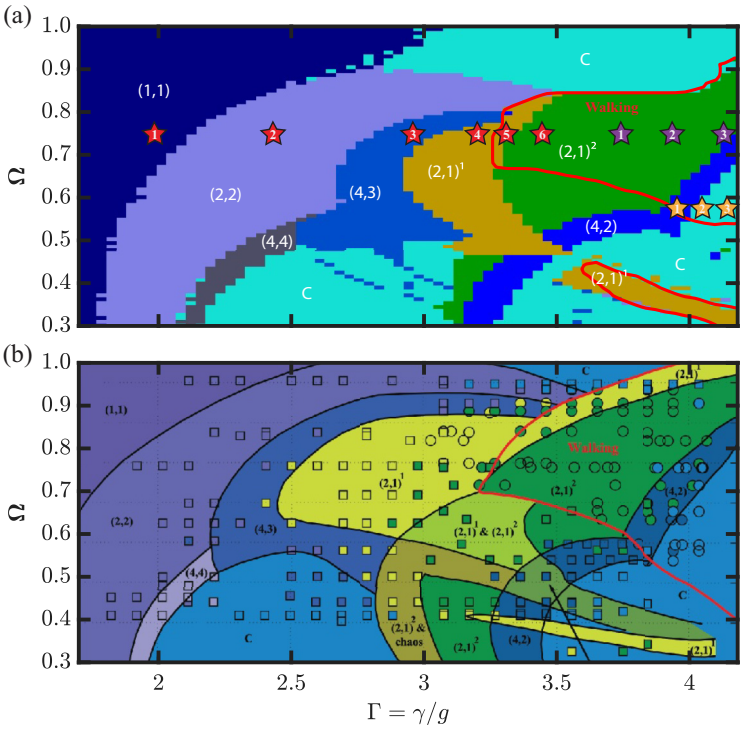

FIG. 4. (a) The dependence of bouncing and walking modes on the vibration number, $\Omega = \omega/\omega_D$, and the bath acceleration, $\Gamma = \gamma/g$, for a bath of 20 cSt silicone oil driven at $f = 80$ Hz, obtained with our theoretical model by sweeping down from $\Gamma = 4.18$ to $\Gamma = 1.7$. (b) The equivalent regime diagram reproduced from Wind-Willassen *et al.* [14] with permission. In (b) the squares and circles denote experimentally observed bouncing and walking modes, respectively. The walking region and various mode transitions are accurately captured by our model. The red, purple, and yellow stars correspond to different (Γ, Ω) pairs that will be the focus of our energetic analysis.

flips arise, so the drop proceeds in a single direction. Conversely, the second chaotic mode exhibits frequent π-phase flips (over a characteristic time $\sim 1000 T_F$), and associated reversals in the walking direction. In this state, the associated impact phases are more widely distributed. We note that for unidirectional motion without phase flipping, whether an impact accelerates or decelerates the drop is determined by whether the phase of impact lies inside or outside the interval $[\pi/2, 3\pi/2]$.

We use the phase information so deduced to identify the dependence of the drop's bouncing mode (n_p, n_b) on the drop vibration number, Ω, and the nondimensional vibrational acceleration, $\Gamma = \gamma/g$ [13]. The regime diagram obtained with our model is depicted in Fig. 4(a), and is compared with the regime diagram reported in Wind-Willassen *et al.* [14]. The squares and circles in Fig. 4(b) indicate the experimental results reported by Wind-Willassen *et al.* [14]. We observe a similar partition between modes, with each mode occupying a similar region in parameter space. The region of parameter space in which both $(2, 1)^1$ and $(2, 1)^2$ modes appear in Fig. 4 can be rationalized with our model as emerging from hysteresis. Specifically, the boundary between the two depends on whether Γ is increasing or decreasing. The region of parameter space in which droplets walk, delimitated by the red curve, is also accurately captured by our model.

The regime diagrams presented in Fig. 4 were obtained by sweeping down in memory: for each value of Ω we initialize our simulation at the highest value of Γ, specifically $0.995\Gamma_F$, and progressively decrease this value. It has previously been reported experimentally that the pilot-wave system is prone to hysteresis [3,13,14]: the emerging dynamical states may depend on the

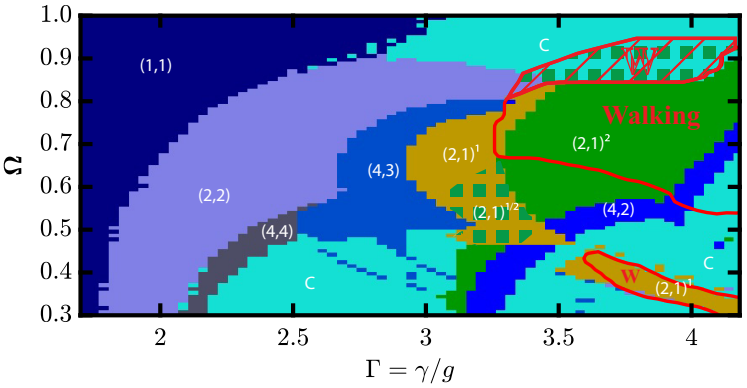

FIG. 5. The dependence of bouncing and walking modes on the vibration number, $\Omega = \omega/\omega_D$, and the bath acceleration, $\Gamma = \gamma/g$, for a bath of 20 cSt silicone oil driven at $f = 80$ Hz, obtained with our theoretical model by sweeping up from $\Gamma = 1.7$ to $\Gamma = 4.18$. The striped or checked regions indicate the presence of hysteresis, where different results were obtained by sweeping up or down in Γ (see Fig. 4). The red striped (green-blue checked) region in the upper right indicates the region where the $(2, 1)^2$ walking mode obtains when sweeping down, while a chaotic bouncing mode arises when sweeping up. The green-yellow checked region indicates the coexistence of the $(2, 1)^1$ and $(2, 1)^2$ states that arise depending on whether one is sweeping up or down in Γ.

initialization. As this hysteresis has not previously been characterized in detail, we will do so here. We thus repeat our simulations by starting from the lowest Γ value, then increasing it progressively.

In Fig. 5 we observe that certain regions of the regime diagram are prone to hysteresis, especially at relatively high memory ($\Gamma > 3$) and large drop size ($\Omega > 0.85$). The hysteresis is most pronounced in the top-right corner, where the $(2, 1)^2$ walking mode extends to much larger Ω when sweeping down in memory. In the center of the diagram, there is also a region where the $(2, 1)^1$ mode is more prevalent when sweeping up, while $(2, 1)^2$ is likewise when sweeping down. More generally, the value of Γ at each mode transition is approximately $\Delta\Gamma \approx 0.1$ higher when sweeping up than down.

III. ENERGETIC CHARACTERIZATION OF DROPLET AND PILOT WAVE

We now derive expressions for the wave and droplet energies. The droplet (or "particle") energy, $\overline{E}_p$, can be simply expressed as the sum of its potential and kinetic energy, time-averaged over an appropriate interval,

$$\overline{E}_p = \langle E_p \rangle = \left\langle mgz_p + \tfrac{1}{2}m\dot{z}_p^2 + \tfrac{1}{2}m|\dot{\boldsymbol{x}}_p|^2 \right\rangle, \tag{6}$$

where the brackets denote time averages. When the droplet is in a periodic (n_p, n_b) mode, we average over the periodicity of the motion, specifically $n_p T_F$. When the droplet is in a chaotic bouncing or walking state, since its vertical dynamics do not have a definite period, we average over a sufficiently long time for the energetics to converge, typically $2000T_F$.

For sufficiently large vibrational forcing, the wave field generated by the droplet can be treated as quasi-inviscid [43], and as undergoing a simple exchange between its kinetic energy and its gravitational potential and surface energies. Therefore, we adopt the definition of gravitational potential and surface energies for small-amplitude waves ($|\nabla h| \ll 1$) from Moláček and Bush [13] in order to deduce the total wave energy

$$\overline{E} = \langle E \rangle = \left\langle \iint_{\mathbb{R}^2} \frac{1}{2}\rho g h^2(\boldsymbol{x}, t)\, \mathrm{d}\boldsymbol{x} + \iint_{\mathbb{R}^2} \frac{\sigma}{2}|\nabla h(\boldsymbol{x}, t)|^2\, \mathrm{d}\boldsymbol{x} \right\rangle. \tag{7}$$

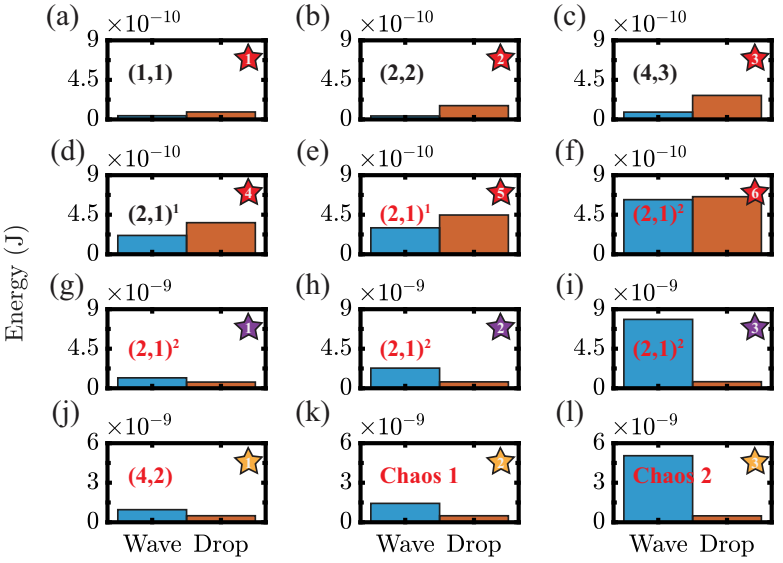

FIG. 6. Partitioning between wave and drop energy as defined in Eqs. (6) and (7), respectively. Panels (a)–(f) correspond to the red stars in Fig. 4 (at $\Omega = 0.76$) in increasing order of vibrational forcing, γ/γ_F. Both energies increase monotonically with vibrational forcing, with the wave energy jumping substantially following establishment of the resonant $(2, 1)^1$ state, and even more so for the relatively energetic $(2, 1)^2$ state. Panels (g)–(i) correspond to the purple stars in Fig. 4 (at $\Omega = 0.76$) and illustrate the most energetic $(2, 1)^2$ walking mode. Panels (j)–(l) correspond to the yellow stars in Fig. 4 (at $\Omega = 0.55$) whose dynamics are described in Figs. 3(c)–3(e). Notably, the transition from resonant to chaotic walking [(j)–(l)] does not substantially diminish the energy: the wave energy dominates the droplet energy even in the most chaotic walking state.

Notably, the spatial damping in the wave kernel, $\mathscr{K}(|\boldsymbol{x}|)$ [see Eq. (4)], ensures that the surface integrals converge. Using Eqs. (6) and (7) for the drop and wave energies, we proceed by investigating their dependence on the relevant control parameters, Γ and Ω. We begin by characterizing the energy partitioning for different drops of a fixed size ($\Omega = 0.76$ and $\Omega = 0.55$) and for increasing vibrational acceleration Γ. The relevant points are indicated by stars in Fig. 4.

Figures 6(a)–6(f) indicate that the drop energy, $\overline{E}_p$, increases monotonically with memory, with a notable jump arising at the transition between $(2, 1)^1$ and $(2, 1)^2$ walking modes. The wave energy is relatively low for the (1,1), (2,2), and (4,3) modes, for which resonance with the subharmonic Faraday waves has yet to be achieved. It increases with the onset of resonance in the $(2, 1)^1$ bouncing state, and substantially more with the transition to walking and to the most energetic $(2, 1)^2$ mode. Figures 6(g)–6(i) depict in greater detail the system's most energetic $(2, 1)^2$ walking mode. In panel (i), at $\gamma/\gamma_F = 0.99$, the maximum energy state is achieved, where the wave energy exceeds the drop energy by a factor of approximately 10.

Figures 6(j)–6(l) characterize the energetic behavior at high memory for relatively small drops $\Omega = 0.55$, following transition from a resonant (4,2) mode into chaos. One might expect the loss of resonance and emergence of chaos to decrease the system's wave energy, owing to destructive interference in the wave field, but such is not the case. The (4,2) mode (j), arising at $\gamma/\gamma_F = 0.935$, has the lowest wave energy despite being in resonance with its pilot wave, as is apparent in Fig. 3. In Figs. 6(k) and 6(l), we depict two chaotic modes. The first occurs at $\gamma/\gamma_F = 0.965$, where there is still some structure to the impact phase distribution, and the droplet moves in a single direction. The impact phases are still concentrated around that of the resonant $(2, 1)^2$ walker, so its wave field is not greatly affected. Despite perfect resonance being lost, the increase in memory induces an increase in wave energy, owing to the associated diminution of wave damping. The second chaotic mode arises

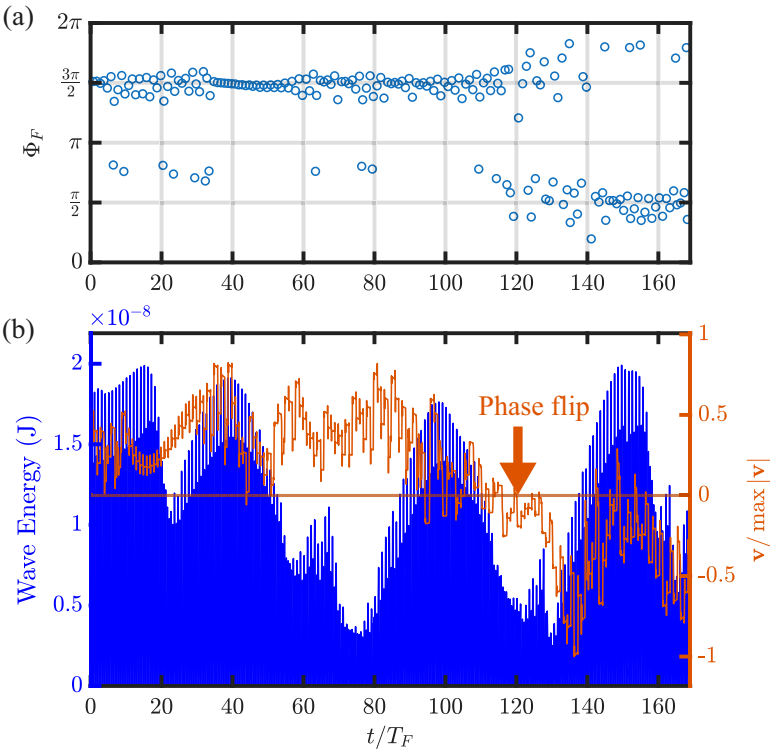

FIG. 7. Time evolution of (a) the droplet bouncing phase and (b) horizontal speed (red) and wave energy (blue) in the chaotic regime corresponding to Fig. 6(l), in which a drop moves along a line. Note the exchange between droplet kinetic energy and wave energy. The droplet phase flip occurring for $t/T_F \sim 120$ is followed by destructive interference and a reduction of wave energy. The wave energy begins to recover after $t/T_F \sim 130$, when the drop resumes its walking motion in the opposite direction.

at $\gamma/\gamma_F = 0.995$, where there is a broader distribution of impact phases and the droplet frequently reverses direction. One might expect that destructive interference due to the chaotic impact phases and reversals of direction of the drop would lower the wave energy through wave interference, but the higher vibrational acceleration has the dominant effect on the droplet's wave energy.

The chaotic walker in Fig. 6(k) spontaneously undergoes many phase flips and reversals in direction as it walks along a line. Figure 7 illustrates one such reversal. At $t/T_F \sim 120$, the drop slows down, initiating a phase-flipping event. The resulting destructive wave interference prompts a decrease in the wave energy. As the phase flip and associated jittering behavior end ($t/T_F \sim 130$), the drop resumes its motion, now in the opposite direction, and the wave field begins to build up again.

In Fig. 8 we present a more complete characterization of the system energetics. Specifically, we sweep the entire parameter space (γ/γ_F, Ω) and compute the energy contour plots for both wave and droplet energy. The droplet energy contour plot in Fig. 8(a) is presented with a linear scale and the wave energy in Fig. 8(b) with logarithmic scale, as necessitated by the exponential increase of the wave energy with memory. Recall that the temporal damping term is prescribed by $e^{-(t-t_i)/(T_F \mathrm{Me})}/\sqrt{t-t_i}$ where $\mathrm{Me} = T_D/[T_F(1-\gamma/\gamma_F)]$ [12]. Therefore, at high memory, where the majority of the hydrodynamic quantum analogs emerge, the wave energy dominates the droplet energy by up to a factor of 10. For the droplet energy, $\overline{E}_p$, the dominant exchange occurs between gravitational potential energy and vertical kinetic energy: the horizontal kinetic energy is typically smaller by an order of magnitude.

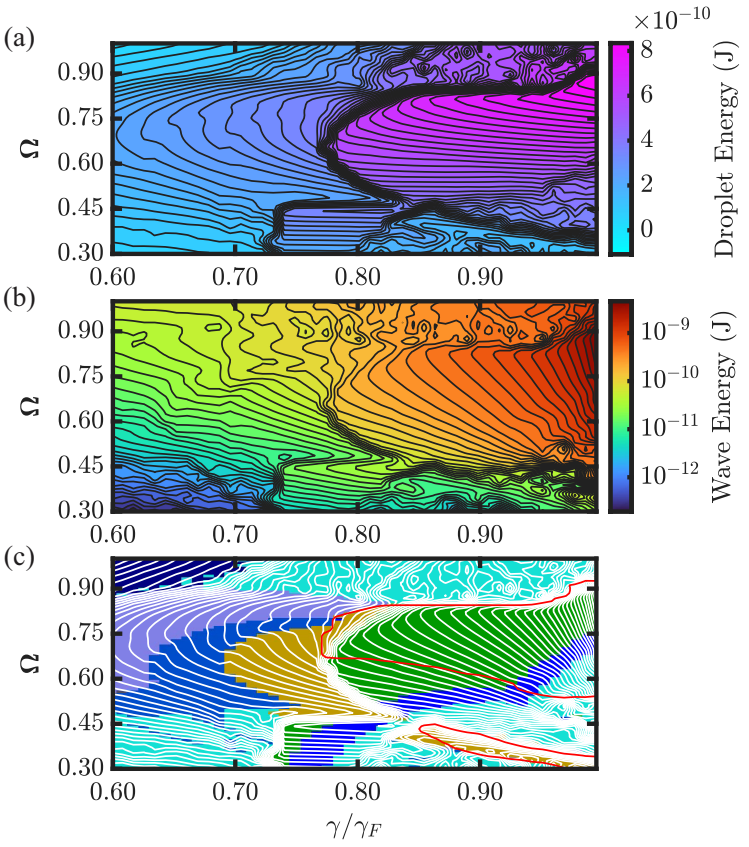

FIG. 8. Contour plots illustrating the dependence on vibrational forcing γ/γ_F and vibration number Ω of (a) droplet energy, (b) wave energy, and (c) total energy for drops on a bath of 20 cSt silicone oil driven at $f = 80$ Hz. Plots were obtained by sweeping upward from $\gamma/\gamma_F = 0.6$ to $\gamma/\gamma_F = 0.995$. In (a) and (b), both wave and droplet energy increase monotonically with γ/γ_F, especially the wave energy, which dominates at high memory. (c) Overlay of the total-energy contour lines (white curves) onto the regime diagram [Fig. 4(a)]. Total-energy contour levels are evenly spaced in logarithmic scale between 10^{-12} J and 10^{-8} J. The $(2, 1)^1$ to $(2, 1)^2$ transition coincides with a large energy jump. The total energy peaks for $(2, 1)^2$ walkers near the Faraday threshold. In such states the wave energy exceeds the drop energy by a factor of 5 to 10.

In Fig. 8(c) the overlay of the total energy contour lines with our regime diagram allows us to identify how the mode transitions impact the system energy. We observe that the largest increase in energy occurs at the $(2, 1)^1$ to $(2, 1)^2$ transition. This reinforces the notion that $(2, 1)^2$ is the most energetic mode [13], and that the transition between the $(2, 1)^1$ to $(2, 1)^2$ is not only a transition into a relatively fast walking state but also into the walker's most energetic state. The energy peaks for large $(2, 1)^2$ walkers near the Faraday threshold, as seen in the top right of Fig. 8(c). Smaller drops at equivalent vibrational forcing (shift from  to  in Fig. 4) lose resonance and transition into chaotic walking states, decreasing the net energy. This behavior is consistent with the physical picture presented in Fig. 7, and reinforces the notion that nonresonant effects enhance destructive interference, so slow the divergence of the wave energy with increasing memory.

IV. STROBED ENERGETICS

The energetics of pilot-wave hydrodynamics have been studied in the context of the stroboscopic model [23] by Durey and Bush [33]. In the stroboscopic model, one assumes perfect resonance

between the droplet and its pilot wave, averages over its vertical dynamics, and describes only its horizontal dynamics. As impact phase is unspecified in the stroboscopic model, it was assigned a value that provides the best fit for the experimental dependence of walking speed on memory for $(2, 1)^2$ walkers [23]. We proceed by comparing our energetic results to those deduced by Durey and Bush [33], with a view to highlighting the limitations of the stroboscopic model in describing the system energetics. A more detailed comparison with their analytical results is presented in Appendix A.

In the stroboscopic model, the droplet does not fly through the air, but rather surfs on a wave of height H. The associated droplet energy,

$$\overline{E}_{p,\mathrm{str.}} = mgH + \tfrac{1}{2}m|\dot{\boldsymbol{x}}_p|^2,$$

thus does not take account of the vertical dynamics of the droplet, and consists only of its horizontal kinetic energy and the gravitational potential energy, mgH. The height at impact, H, may be computed from our model by averaging the wave height over the impact time,

$$H = \frac{\langle h(\boldsymbol{x}_p, t)F_N(t)\rangle}{\langle F_N(t)\rangle}. \tag{8}$$

We note that the H so computed serves as a proxy for the mean droplet height, $\langle z_p(t)\rangle$, computed in our variable-phase model by averaging over one Faraday period. Furthermore, the energy, $E_{\mathrm{str.}}$, of the stroboscopic wave field is related to the energy of the Faraday wave field averaged over one Faraday period by $\overline{E} = \frac{1}{2}E_{\mathrm{str.}}/\mathscr{C}^2$ [33], where $\mathscr{C}$ is the phase of impact relative to the wave oscillation [see Eq. (B2)]. The parameters $\sin\Phi$ and $\mathscr{C}$ in the stroboscopic model are chosen to ensure consistency with the simulations. In particular, $\sin\Phi = 0.27$ is chosen to match the walking threshold and $\mathscr{C} = 0.24$ to match the corresponding wave energy.

Figure 9 presents a comparison between the droplet gravitational potential energies mgH and $mg\langle z_p(t)\rangle$. The most illuminating comparison is expected to arise in the region of parameter space where $(2, 1)^2$ walkers obtain. In this regime, $mg\langle z_p(t)\rangle$ increases with memory, while the opposite is true for mgH. The latter trend is consistent with the observation of Oza *et al.* (Fig. 3 of [23]) that as γ/γ_F increases, the droplet rides lower on its pilot wave. Our consideration of the vertical dynamics reveals that despite this trend, the drop actually flies higher, so that its average gravitational potential energy increases monotonically with memory. This result highlights the fact that, through neglecting the vertical drop dynamics, the stroboscopic model captures an incomplete picture of the dependence of gravitational potential energy on vibrational forcing.

Figure 9 also illustrates that, when the droplet is in the $(2, 1)^2$ mode, the wave energy increases monotonically with memory, according to both the stroboscopic model and our full model. However, the variable-phase model also captures the transitions between $(2, 1)^1$, $(2, 1)^2$ and (4,2) walkers. The assumption of constant impact phase in the stroboscopic model precludes its capturing the abrupt increase in walking speed prompted by the transition from the $(2, 1)^1$ to $(2, 1)^2$ modes [23] [see black curves in Figs. 9(a) and 9(b)]. Our variable-phase model does capture the trend reported experimentally [13] [Fig. 9(a)], that the walking speed increases monotonically in the $(2, 1)^1$ mode, before the transition to a $(2, 1)^2$ mode where the walking speed is nearly constant with respect to memory.

V. DISCUSSION AND CONCLUSIONS

The use of the nonresonant model of Primkulov *et al.* [16] has allowed for consideration of the vertical drop dynamics in the system energetics. We began by benchmarking our theoretical model against existing regime diagrams. We then characterized the partitioning of energy between wave and droplet, and characterized how this partitioning changes with the vibrational forcing of the system. The wave energy dominates at high memory: in the high-memory ($\mathrm{Me} \gg 1$) parameter regime of interest in hydrodynamic quantum analog experiments [6], the wave energy is typically larger that the droplet's by a factor of 5 to 10. Furthermore, the droplet's horizontal kinetic energy

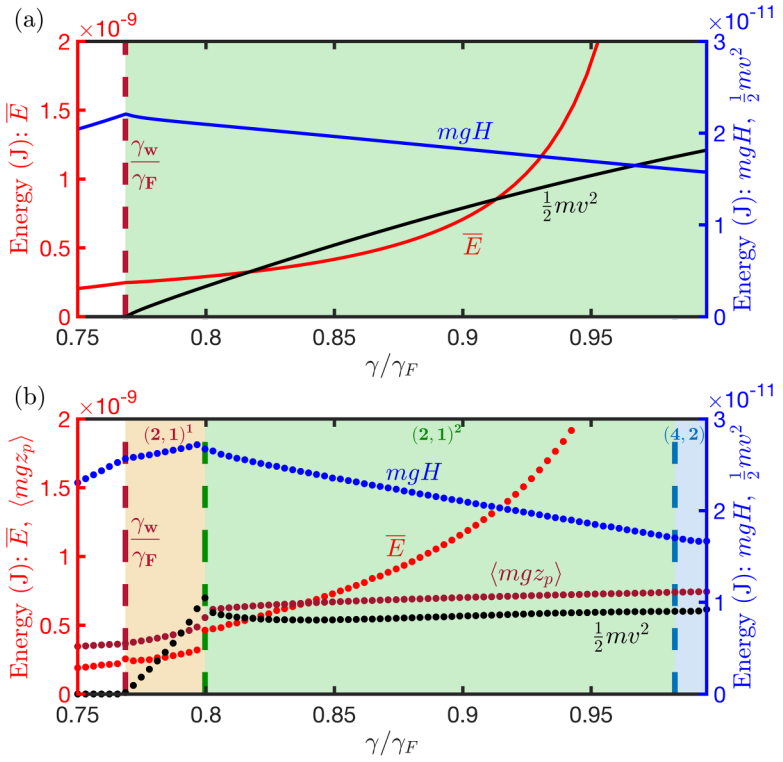

FIG. 9. Comparison to the stroboscopic model. The dependence of energy on the vibrational forcing, γ/γ_F, for walkers of size $\Omega = 0.76$, corresponding to the red and purple stars in Fig. 4. (a) The results obtained from the stroboscopic model [33] with constant impact phases $\sin\Phi = 0.27$ and $\mathscr{C} = 0.24$ chosen to match the vibrational acceleration and wave energy of the numerical simulations at the walking threshold, γ_w. (b) The results of the numerical simulation of our model. We compare the wave energy ($\overline{E}$, red), mean ($\langle mgz_p \rangle$, maroon) and stroboscopic (mgH, blue) gravitational potential energies, and the droplet's horizontal kinetic energy ($\frac{1}{2}m|\dot{\boldsymbol{x}}_p|^2$, black). Within the region of $(2,1)^2$ walking, the qualitative behavior of the wave and stroboscopic gravitational potential energies predicted by the stroboscopic model is captured by our nonresonant model.

is negligible with respect to the other system energies even at the highest walking speeds. The total energy retained in the droplet and pilot wave is maximized for the largest $(2,1)^2$ walkers, with both wave and droplet energy reaching their peak near the Faraday threshold. However, contrary to expectations, breaking resonance between drop and pilot wave does not substantially reduce the wave energy, even when the droplet enters a highly chaotic mode: provided that the vibrational forcing is sufficiently high, the wave energy still increases with memory. We thus surmise that the destructive wave interference arising in the highly chaotic states is more than offset by the increased persistence of the wave field arising near the Faraday threshold.

By comparing to the predictions of the stroboscopic model energetic results [33], we have assessed the contribution of the droplet's vertical dynamics on the energetic landscape. The impact height of the droplet on its pilot wave provides an incomplete picture of the droplet's gravitational potential energy, as the impact height and average height of flight of the drop over a Faraday period follow opposite trends. With increasing memory the drop rides increasingly low on its pilot wave, but flies higher: drop potential energy thus increases. Our variable-phase model has also clarified the changes in system energetics associated with the transitions between various bouncing and walking modes.

TABLE II. Analogy between the energetics of the walker system and de Broglie's double solution pilot-wave theory of quantum dynamics. The hydrodynamic system is marked by the same dominant balance between internal particle energy and wave energy suggested by de Broglie [1,4,5].

	Double solution pilot-wave theory	Hydrodynamic pilot-wave system
Vibration frequency	$\omega_c = mc^2/\hbar$	$\omega_d \sim \sqrt{\sigma/m} \sim \omega_F$
Waves and wavelength	Matter waves, λ_B	Faraday waves, λ_F
Internal energy	mc^2	$\langle mgz_p(t)\rangle$
Wave energy	$\hbar\omega$	$\overline{E}$ (7)
Kinetic energy	pc	$\frac{1}{2}m\lvert\dot{\boldsymbol{x}}_p\rvert^2$
Dominant energy balance	$mc^2 \leftrightarrow \hbar\omega$	$\langle mgz_p(t)\rangle \leftrightarrow \overline{E}$

Pilot-wave hydrodynamics provide a physical picture reminiscent of de Broglie's double solution pilot-wave theory [4], and our study allows us to deepen the analogy between the two systems [1]. De Broglie posited that particles undergo internal vibration at the Compton frequency, and in so doing generate a monochromatic pilot wave with the de Broglie wavelength. The droplet's vertical dynamics can then be identified with an internal vibration, and the resulting Faraday waves with de Broglie's matter waves. De Broglie also posited an exchange between the particle rest-mass energy, mc^2, and its wave field energy, $\hbar\omega$ [44]. The relativistic energy-momentum relation obtained from the Klein-Gordon equation, $(\hbar\omega)^2 = (pc)^2 + (mc^2)^2$ (with p being the particle momentum), expresses a dominant exchange between the wave energy, $\hbar\omega$, kinetic anergy, pc, and rest-mass energy, mc^2. In our system, we can identify the drop's wave energy with $\hbar\omega$, the drop's gravitational potential energy with the internal energy mc^2, and the droplet's horizontal kinetic energy with pc. The dominant energy exchange is between the droplet's "internal energy" and the wave field, with the kinetic energy of the droplet being relatively small. The analogy with de Broglie's double solution pilot-wave theory is summarized in Table II.

Our analysis of the energetics of pilot-wave hydrodynamics has enabled us to test our preconceptions about the walking droplet system and its energetics, and opened the door to future exploration. For example, it should now be possible to assess whether the emergence of quantized states in orbital dynamics [22,27] and lattices [41], as well as the emergence of coherent statistical states [45,46], can be rationalized energetically.

ACKNOWLEDGMENTS

The authors thank Joel Been for valuable discussions. J.W.M.B. gratefully acknowledges funding from the National Science Foundation through Grant No. CMMI- 2154151 and the Office of Naval Research through Grant No. N00014-24-1-2232.

DATA AVAILABILITY

There are no publicly available research data or software supporting this paper. Requests for further information or data should be sent to the authors.

APPENDIX A: COMPARISON TO THE STROBOSCOPIC MODEL

The stroboscopic model follows from time-averaging Eqs. (3) and (4) over one Faraday period, and noting that the vertical force balance requires that $\int_{T_F} F_N(t)\,\mathrm{d}t = mgT_F$, which also reduces the horizontal drag coefficient to a single constant denoted by D. Moreover, for the sake of algebraic simplicity, the term $1/\sqrt{t-t_i}$ appearing in the wave height expression from (4) is approximated by $1/\sqrt{T_F}$. On the basis of this stroboscopic approximation, Durey and Bush [33] deduced simple relationships between the droplet's gravitational potential energy, wave energy, and walking speed,

which serve here as valuable points of comparison. Specifically, for steady dynamical states, where the stroboscopic energies are constant in time, they deduced the relationships

$$\frac{H}{H_B} = \gamma_D(|\dot{\boldsymbol{x}}_p|) \quad \text{and} \quad \frac{H}{H_B} = \frac{\overline{E}}{\overline{E}_B}. \tag{A1}$$

In Eq. (A1), $\gamma_D(v) = 1 - v^2/c^2$ is a diminution factor that depends on the relative magnitude of the walking speed, v, and $c = \sqrt{mgA/DT_F}$ the maximum walker speed arising in the high memory limit, $\gamma \to \gamma_F$ [23]. The factor A corresponds to the amplitude of the surface wave induced by a single impact, and so depends on the droplet's impact phase. Finally, H_B and $\overline{E}_B$ are the respective energies computed from the wave field generated by a droplet bouncing in place at the origin with the same vertical motion as the simulated walker. Specifically, the wave field for this bouncing state, denoted $h_B(|\boldsymbol{x}|)$, is defined using the computed reaction force, $F_N(t)$, corresponding to the simulated walker at the same point (Γ, Ω) in parameter space.

For periodic vertical motion in the (2,1) mode, the impact phase computed from each numerical simulation is fed into the stroboscopic energy formulas (A1) via the wave field $h_B(|\boldsymbol{x}|)$. However, neglecting the $1/\sqrt{t - t_i}$ term in the stroboscopic model leads to a wave field whose amplitude differs from that of the vertical dynamics model by a factor of approximately 2 [35]. To partially correct this inconsistency between the nonresonant and stroboscopic models, and thus our computation of A and c, we deduce the stroboscopic bouncer wave field from our equations, retaining the $1/\sqrt{t - t_i}$ dependence present in our model, and then choose A to match the amplitude of the bouncer wave field prescribed by the conventional integral stroboscopic bouncer wave field definition [23,35], as outlined in Appendix B.

We can now assess the validity of Eqs. (A1) in the context of the nonresonant model, for which the vertical dynamics are also considered. When confining our attention to the range $\gamma/\gamma_F = 0.775$ to 0.97 of the predominant $(2, 1)^1$ and $(2, 1)^2$ walking modes, a reasonable approximation to the relationship $\overline{E}/\overline{E}_B = H/H_B$ is observed, as depicted in Figs. 10(a) and 10(c). However, the profile of $\gamma_D(|\dot{\boldsymbol{x}}_p|)$ looks vastly different in the nonresonant model when compared to the stroboscopic case, highlighting the shortcomings of the stroboscopic prediction $H/H_B = \gamma_D(|\dot{\boldsymbol{x}}_p|)$, as illustrated in Figs. 10(b) and 10(d).

APPENDIX B: MATCHING THE WAVE AMPLITUDE

Under the stroboscopic assumptions of subharmonic, periodic steady-state dynamics, when averaging over a Faraday period the wave field (4) becomes

$$\overline{h}(\boldsymbol{x}, t) = \mathscr{C}\overline{\eta}(\boldsymbol{x}, t), \tag{B1}$$

with

$$\mathscr{C} = \frac{\int_{T_F} F_N(s)\cos(\omega_F s)\,\mathrm{d}s}{\int_{T_F} F_N(s)\,\mathrm{d}s} \tag{B2}$$

the phase of impact relative to the wave oscillation. In (B1), $\overline{\eta}(\boldsymbol{x}, t)$ is the slowly varying envelope, and we have averaged over the fast timescale oscillations, where $h(\boldsymbol{x}, t) = \cos(\omega_F t)\overline{\eta}(\boldsymbol{x}, t)$. Therefore,

$$\overline{\eta}(\boldsymbol{x}, t) = \sum_{i=1}^{n} A_i \frac{\mathrm{e}^{-(t-t_i)/(T_F \mathrm{Me})}}{\sqrt{t - t_i}} \mathscr{H}(|\boldsymbol{x} - \boldsymbol{x}_i|)\,. \tag{B3}$$

For stationary bouncing at the origin, $t_i = iT_F$ and $\boldsymbol{x}_i = \boldsymbol{0}$. Furthermore, the force balance over a Faraday period allows us to note that $A_i = \widetilde{A}$, where

$$\widetilde{A} = \sqrt{2\mu_e/\pi\rho}\,\frac{mgk_F^3 T_F \mathscr{S}}{3k_F^2\sigma + \rho g} \tag{B4}$$

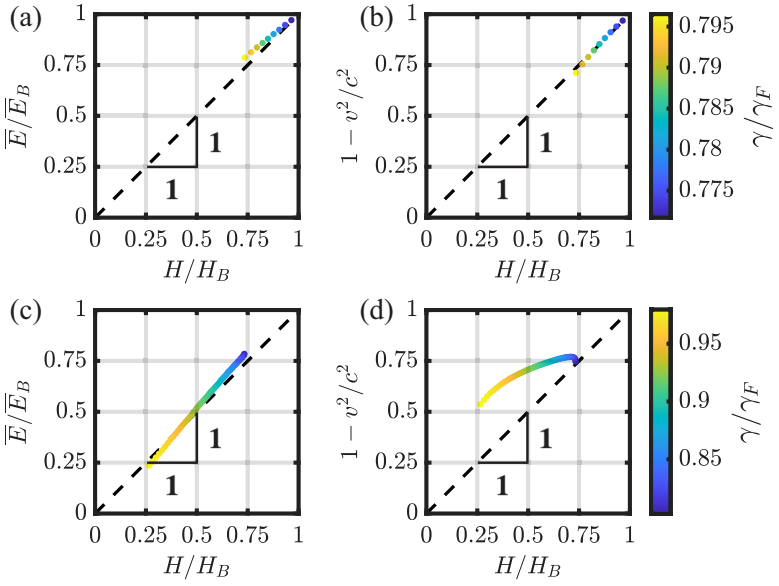

FIG. 10. The dependence on H/H_B of $\overline{E}/\overline{E}_B$ (left column) and $1-v^2/c^2$ (right column) for walking in the (a), (b) $(2,1)^1$ and (c), (d) $(2,1)^2$ modes. The black dashed lines represent the stroboscopic model predictions from Eq. (A1), and the colored curves represent the results of our numerical simulations. Both the wave energies and impact heights behave similarly in the stroboscopic and nonresonant models, leading in (a) and (c) to a qualitative agreement of our model with the relationship $H/H_B = \overline{E}/\overline{E}_B$ in Eq. (A1). The discrepancy in (d) reflects the shortcomings of the stroboscopic approximation, specifically the neglect of the $1/\sqrt{t-t_i}$ term in the wave kernel and the inability to resolve the vertical dynamics. The relationship $H/H_B = 1-v^2/c^2$ in Eq. (A1) is thus not captured with our more complete model.

and

$$\mathscr{S} = \frac{\int_{T_F} F_N(s)\sin(\omega_F s)\,\mathrm{d}s}{\int_{T_F} F_N(s)\,\mathrm{d}s}$$

is a phase parameter quantifying the efficiency of wave generation. So finally, we obtain

$$h_B(|\boldsymbol{x}|) = \overline{A}\mathscr{H}(|\boldsymbol{x}|)\sum_{i=1}^{\infty}\frac{\mathrm{e}^{-i/\mathrm{Me}}}{\sqrt{i}}, \tag{B5}$$

where

$$\overline{A} = \sqrt{\frac{\mu_e T_F}{2\pi\rho}}\frac{mgk_F^3\sin\Phi}{3k_F^2\sigma+\rho g}$$

and $\sin\Phi = 2\mathscr{S}\mathscr{C}$ [13].

On the other hand, the integral expression using a quasistatic approximation for the stroboscopic wave field employed by Durey and Bush [33] is given by [23,35]

$$h_{B,\mathrm{str.}}(|\boldsymbol{x}|) = \frac{A}{T_F}\int_{-\infty}^{t}\mathscr{H}(|\boldsymbol{x}|)\mathrm{e}^{-(t-s)/T_M}\,\mathrm{d}s = A\mathrm{Me}\,\mathscr{H}(|\boldsymbol{x}|), \tag{B6}$$

where $T_M = T_F\mathrm{Me}$ is the wave decay time. Matching A for the amplitude of the wave field of a bouncer such that $h_B(|\boldsymbol{x}|) = h_{B,\mathrm{str.}}(|\boldsymbol{x}|)$ yields

$$A = \frac{\overline{A}}{\mathrm{Me}} \sum_{i=1}^{\infty} \frac{\mathrm{e}^{-i/\mathrm{Me}}}{\sqrt{i}}, \tag{B7}$$

which defines A, and thus c, for the stroboscopic model.

[1] J. W. M. Bush, Pilot-wave hydrodynamics, Annu. Rev. Fluid Mech. **47**, 269 (2015).

[2] Y. Couder, S. Protière, E. Fort, and A. Boudaoud, Walking and orbiting droplets, Nature (London) **437**, 208 (2005).

[3] S. Protière, A. Boudaoud, and Y. Couder, Particle-wave association on a fluid interface, J. Fluid Mech. **554**, 85 (2006).

[4] L. de Broglie, Recherches sur la théorie des quanta, Ph.D. thesis, Université de Paris, Paris, 1924; Ann. Phys. **10**, 22 (1925).

[5] L. de Broglie, Interpretation of quantum mechanics by the double solution theory, Ann. Fondation Louis de Broglie **12**, 1 (1987).

[6] J. W. M. Bush and A. U. Oza, Hydrodynamic quantum analogs, Rep. Prog. Phys. **84**, 017001 (2021).

[7] J. W. M. Bush, V. Frumkin, and P. J. Sáenz, Perspectives on pilot-wave hydrodynamics, Appl. Phys. Lett. **125**, 030503 (2024).

[8] T. Benjamin and F. Ursell, The stability of the plane free surface of a liquid in vertical periodic motion, Proc. R. Soc. A **225**, 505 (1954).

[9] J. W. Miles and D. Henderson, Parametrically forced surface waves, Annu. Rev. Fluid Mech. **22**, 143 (1990).

[10] Y. Couder, E. Fort, C.-H. Gautier, and A. Boudaoud, From bouncing to floating: Noncoalescence of drops on a fluid bath, Phys. Rev. Lett. **94**, 177801 (2005).

[11] D. Terwagne, N. Vandewalle, and S. Dorbolo, Lifetime of a bouncing droplet, Phys. Rev. E **76**, 056311 (2007).

[12] A. Eddi, E. Sultan, J. Moukhtar, E. Fort, M. Rossi, and Y. Couder, Information stored in Faraday waves: The origin of a path memory, J. Fluid Mech. **674**, 433 (2011).

[13] J. Moláček and J. W. M. Bush, Drops walking on a vibrating bath: Towards a hydrodynamic pilot-wave theory, J. Fluid Mech. **727**, 612 (2013).

[14] Ø. Wind-Willassen, J. Moláček, D. M. Harris, and J. W. M. Bush, Exotic states of bouncing and walking droplets, Phys. Fluids **25**, 082002 (2013).

[15] J. Moláček and J. W. M. Bush, Drops bouncing on a vibrating bath, J. Fluid Mech. **727**, 582 (2013).

[16] B. K. Primkulov, D. J. Evans, J. B. Been, and J. W. M. Bush, Nonresonant effects in pilot-wave hydrodynamics, Phys. Rev. Fluids **10**, 013601 (2025).

[17] S. Perrard, E. Fort, and Y. Couder, Wave-based Turing machine: Time reversal and information erasing, Phys. Rev. Lett. **117**, 094502 (2016).

[18] S. Perrard, M. Labousse, M. Miskin, E. Fort, and Y. Couder, Self-organization into quantized eigenstates of a classical wave-driven particle, Nat. Commun. **5**, 3219 (2014).

[19] S. Perrard, M. Labousse, E. Fort, and Y. Couder, Chaos driven by interfering memory, Phys. Rev. Lett. **113**, 104101 (2014).

[20] E. Fort, A. Eddi, A. Boudaoud, J. Moukhtar, and Y. Couder, Path-memory induced quantization of classical orbits, Proc. Natl. Acad. Sci. USA **107**, 17515 (2010).

[21] D. M. Harris and J. W. M. Bush, Drops walking in a rotating frame: From quantized orbits to multimodal statistics, J. Fluid Mech. **739**, 444 (2014).

[22] M. Labousse, A. U. Oza, S. Perrard, and J. W. M. Bush, Pilot-wave dynamics in a harmonic potential: Quantization and stability of circular orbits, Phys. Rev. E **93**, 033122 (2016).

[23] A. U. Oza, R. R. Rosales, and J. W. M. Bush, A trajectory equation for walking droplets: Hydrodynamic pilot-wave theory, J. Fluid Mech. **737**, 552 (2013).
[24] D. M. Harris, J. Quintela, V. Prost, P.-T. Brun, and J. W. M. Bush, Visualization of hydrodynamic pilot-wave phenomena, J. Vis. **20**, 13 (2017).
[25] M. Durey and J. W. M. Bush, Classical pilot-wave dynamics: The free particle, Chaos **31**, 033136 (2021).
[26] M. Durey and P. A. Milewski, Faraday wave–droplet dynamics: Discrete-time analysis, J. Fluid Mech. **821**, 296 (2017).
[27] A. U. Oza, D. M. Harris, R. R. Rosales, and J. W. M. Bush, Pilot-wave dynamics in a rotating frame: On the emergence of orbital quantization, J. Fluid Mech. **744**, 404 (2014).
[28] A. U. Oza, Ø. Wind-Willassen, D. M. Harris, R. R. Rosales, and J. W. M. Bush, Pilot-wave hydrodynamics in a rotating frame: Exotic orbits, Phys. Fluids **26**, 082101 (2014).
[29] C. Borghesi, J. Moukhtar, M. Labousse, A. Eddi, E. Fort, and Y. Couder, Interaction of two walkers: Wave-mediated energy and force, Phys. Rev. E **90**, 063017 (2014).
[30] N. Liu, M. Durey, and J. W. M. Bush, Pilot-wave dynamics in a rotating frame: The onset of orbital instability, J. Fluid Mech. **973**, A4 (2023).
[31] M. M. P. Couchman and J. W. M. Bush, Free rings of bouncing droplets: Stability and dynamics, J. Fluid Mech. **903**, A49 (2020).
[32] M. Hubert, S. Perrard, N. Vandewalle, and M. Labousse, Overload wave-memory induces amnesia of a self-propelled particle, Nat. Commun. **13**, 4357 (2022).
[33] M. Durey and J. W. M. Bush, The energetics of pilot-wave hydrodynamics, J. Fluid Mech. **1009**, A4 (2025).
[34] A. Eddi, A. Decelle, E. Fort, and Y. Couder, Archimedean lattices in the bound states of wave interacting particles, Europhys. Lett. **87**, 56002 (2009).
[35] M. M. P. Couchman, S. E. Turton, and J. W. M. Bush, Bouncing phase variations in pilot-wave hydrodynamics and the stability of droplet pairs, J. Fluid Mech. **871**, 212 (2019).
[36] C. A. Galeano-Rios, M. M. P. Couchman, P. Caldairou, and J. W. M. Bush, Ratcheting droplet pairs, Chaos **28**, 096112 (2018).
[37] A. U. Oza, E. Siéfert, D. M. Harris, J. Moláček, and J. W. M. Bush, Orbiting pairs of walking droplets: Dynamics and stability, Phys. Rev. Fluids **2**, 053601 (2017).
[38] J. Arbelaiz, A. U. Oza, and J. W. M. Bush, Promenading pairs of walking droplets: Dynamics and stability, Phys. Rev. Fluids **3**, 013604 (2018).
[39] T. Gilet and J. W. M. Bush, The fluid trampoline: Droplets bouncing on a soap film, J. Fluid Mech. **625**, 167 (2009).
[40] S. Protière, Y. Couder, E. Fort, and A. Boudaoud, The self-organization of capillary wave sources, J. Phys.: Condens. Matter **17**, S3529 (2005).
[41] D. J. Evans, B. K. Primkulov, and J. W. M. Bush, Phase control of bouncing droplets and rearrangement of bound states, Phys. Rev. Fluids **11**, 014003 (2026).
[42] B. K. Primkulov, D. J. Evans, V. Frumkin, P. J. Sáenz, and J. W. M. Bush, Diffraction of walking drops by a standing Faraday wave, Phys. Rev. Res. **7**, 013226 (2025).
[43] P. A. Milewski, C. A. Galeano-Rios, A. Nachbin, and J. W. M. Bush, Faraday pilot-wave dynamics: Modelling and computation, J. Fluid Mech. **778**, 361 (2015).
[44] L. de Broglie, The reinterpretation of wave mechanics, Found. Phys. **1**, 5 (1970).
[45] D. M. Harris, J. Moukhtar, E. Fort, Y. Couder, and J. W. M. Bush, Wavelike statistics from pilot-wave dynamics in a circular corral, Phys. Rev. E **88**, 011001(R) (2013).
[46] P. J. Sáenz, T. Cristea-Platon, and J. W. M. Bush, Statistical projection effects in a hydrodynamic pilot-wave system, Nat. Phys. **14**, 315 (2018).